

The Canadian Cluster Comparison Project: weak lensing masses and SZ scaling relations^{*}

Henk Hoekstra^{1,2}, Andisheh Mahdavi³, Arif Babul² and Chris Bildfell²

¹ *Leiden Observatory, Leiden University, PO Box 9513, 2300 RA, Leiden, the Netherlands*

² *University of Victoria, Dept. of Physics & Astronomy, 3800 Finnerty Rd, Victoria, BC V8P 5C2, Canada*

³ *San Francisco State University, Dept. of Physics & Astronomy, 1600 Holloway Avenue, San Francisco, CA 94132*

Accepted. Received; in original form

ABSTRACT

The Canadian Cluster Comparison Project is a comprehensive multi-wavelength survey targeting 50 massive X-ray selected clusters of galaxies to examine baryonic tracers of cluster mass and to probe the cluster-to-cluster variation in the thermal properties of the hot intracluster medium. In this paper we present the weak lensing masses, based on the analysis of deep wide-field imaging data obtained using the Canada-France-Hawaii-Telescope. The final sample includes two additional clusters that were located in the field-of-view. We take these masses as our reference for the comparison of cluster properties at other wavelengths. In this paper we limit the comparison to published measurements of the Sunyaev-Zel’dovich effect. We find that this signal correlates well with the projected lensing mass, with an intrinsic scatter of $12 \pm 5\%$ at $\sim r_{2500}$, demonstrating it is an excellent proxy for cluster mass.

Key words: cosmology: observations – dark matter – gravitational lensing – galaxies: clusters

1 INTRODUCTION

Observational constraints on the various constituents that make up the universe have tightened tremendously in the past decade. However, many puzzles remain, most notably the origin of the accelerated expansion of the universe (e.g., Riess et al. 1998; Perlmutter et al. 1999). Another challenge is to explain the transition from a smooth early universe, as indicated by observations of the cosmic microwave background, to today’s highly structured and complex universe.

Arguably, clusters of galaxies provide one of the most important pieces of this fascinating cosmic puzzle. Galaxy clusters are one of the primary reservoirs of baryons in the local Universe that can be studied using observations spanning the full electromagnetic spectrum. As such, they provide an excellent laboratory for studying the physics affecting the evolution of baryons, at least over the past 10 Gyrs. Finally, the number density of clusters is a sensitive function of key cosmological parameters, including the dark energy equation of state (see e.g., Allen et al. 2011, for a recent review). Hence, there is an active ongoing effort to use clusters as precision probes of these parameters.

The use of clusters as cosmological probes and the study of the baryon physics to explain their observable properties are closely connected. The former requires cluster catalogs with well-defined selection functions that somehow need to be related to predictions. The predictions are based on numerical simulations of cold dark matter. As clusters are discovered through their optical, X-ray or radio properties, it is imperative that we understand the relation between the observables and the underlying dark matter distribution.

Cluster samples are increasing rapidly thanks to optical surveys (e.g., Gladders & Yee 2005; Koester et al. 2007), X-ray studies (e.g., Reiprich & Böhringer 2002; Ebeling et al. 2010) and Sunyaev-Zel’dovich surveys (e.g., Williamson et al. 2011; Marriage et al. 2011). The detection significance correlates with mass and can thus be used as a mass-proxy, which nonetheless needs to be calibrated. This can be done using deep X-ray observations, under the assumption that the intra-cluster medium (ICM) is in hydrostatic equilibrium. There is, however, both theoretical and observational evidence that that X-ray masses tend to be biased low if one assumes hydrostatic equilibrium (e.g., Nagai et al. 2007; Mahdavi et al. 2008, 2012).

To compare the baryonic properties of clusters to the results from numerical simulations, we instead need a direct probe of the (dark) matter distribution. Such a probe exists in the form of weak gravitational lensing: the gravitational potential of the cluster perturbs the paths of pho-

^{*} Based on observations from the Canada-France-Hawaii Telescope, which is operated by the National Research Council of Canada, le Centre National de la Recherche Scientifique and the University of Hawaii.

tons emitted by distant galaxies. As a result, the images of the galaxies appear slightly distorted. The amplitude of the distortion provides us with a direct measurement of the gravitational tidal field, which in turn can be used to map the distribution of dark matter *along the line-of-sight* directly (e.g., Kaiser & Squires 1993). However, comparison with other mass traces does require one to make assumptions about the geometry of the cluster, because weak lensing measures the total mass projected along the line-of-sight.

Weak gravitational lensing is now a well-established technique to study the distribution of matter in the universe. The applications range from the study of galaxy halos (e.g., Hoekstra et al. 2004; Mandelbaum et al. 2006; van Uitert et al. 2011) to the study of large-scale structure (e.g., Hoekstra et al. 2006; Fu et al. 2008; Schrabback et al. 2010). Several developments in the past decade have also led to improvements in the weak lensing studies of galaxy clusters. For instance, the galaxy shapes are not only affected by gravitational lensing, but observational distortions can cause systematic signals that are similar in size. However, extensive tests have shown that techniques can now reach an accuracy of 1–2% (e.g., Heymans et al. 2006; Massey et al. 2007; Bridle et al. 2010; Kitching et al. 2012). Finally, the source redshift distributions, which are required to convert the lensing signal into a physical mass, are now much better known, compared to even a few years ago.

It is possible to derive mass estimates by fitting parametric models to the data, which is the only option if the data extend to small radii (e.g. Smail et al. 1997; Dahle et al. 2002; Cypriano et al. 2004; Jee et al. 2011). This is also relevant for the study of high redshift ($z > 0.6$) clusters, which can only be studied reliably using Hubble Space Telescope observations. At these high redshifts lensing masses are particularly important, because the clusters are expected to be dynamically young. Fortunately the number of high redshift clusters for which weak lensing masses have been determined has increased in recent year. For instance Jee et al. (2011) analysed a sample of 22 $z > 0.9$ clusters and found evidence for an evolution in the normalization of the relation between mass and T_X , the X-ray temperature. Clusters of galaxies, however, may show significant substructure or are not well described by the adopted model, which leads to biases in the mass estimates (Hoekstra et al. 2002). As a consequence, it is important to measure the lensing signal out to large radii, which allows for more direct mass measurements.

This is now possible thanks to wide-field imagers on world-class telescopes. For instance, Hoekstra (2007) presented masses for a sample of 20 X-ray luminous clusters of galaxies that were observed using the CFH12k camera on the Canada-France-Hawaii Telescope (CFHT). As part of the Local Cluster Substructure Survey (LoCuSS), Okabe et al. (2010a) presented results for a sample of 30 clusters with $0.15 < z < 0.3$ using Subaru data. As part of a weak lensing follow-up program of clusters discovered by the South Pole Telescope, High et al. (2012) presented results for an initial sample of 5 clusters observed with the Megacam imager on the Magellan telescope.

To fully exploit the statistical power of cluster surveys, it is timely to increase the sample of clusters for which accurate weak lensing masses are available. In this paper we update the results presented in Hoekstra (2007) and augment the sample with 30 clusters with redshifts

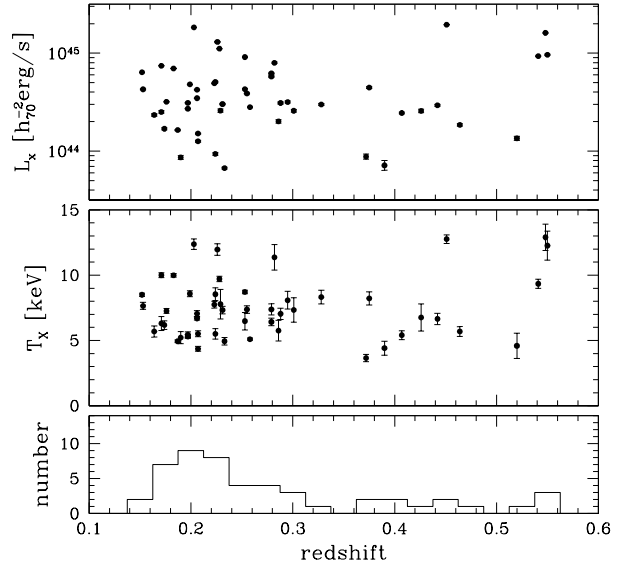


Figure 1. X-ray luminosity within r_{500} in the 2–10 keV band (top) and temperature within r_{2500} (middle) as a function of cluster redshift. The distribution of redshifts is shown in the bottom panel.

$0.15 < z < 0.55$ that were observed using MegaCam on CFHT. This sample forms the basis for the Canadian Cluster Comparison Project (CCCP), which is a comprehensive multi-wavelength study of these massive clusters of galaxies.

The structure of the paper is as follows. In §2 we present the data and discuss the data analysis. The weak lensing analysis is discussed in §3 and the mass measurements are presented in §4. In §5 we compare our results to measurements of the Sunyaev-Zel’dovich Effect. Throughout the paper we assume a cosmology with $\Omega_m = 0.3$, $\Omega_\Lambda = 0.7$ and $H_0 = 70h_{70}$ km/s/Mpc.

2 CLUSTER SAMPLE AND OPTICAL DATA

The main objective of the Canadian Cluster Comparison Project (CCCP) is to study the different baryonic tracers of cluster mass and to explore insights about the thermal properties of the hot diffuse gas and the dynamical states of the clusters that can be gained from cluster-to-cluster variations in these relationships. An important aspect is to compare to accurate weak lensing masses for the clusters, which requires deep data with good image quality over a wide field-of-view, for which we use the Canada-France-Hawaii Telescope (CFHT).

The starting point of the project is the sample of 20 clusters, for which deep archival *B* and *R* band observations with the CFH12k camera were available (the first 20 entries in Table 1). This sample was studied in Hoekstra (2007); Mahdavi et al. (2008). Nearly half of these clusters were originally observed by the Canadian Network for Observational Cosmology (CNOC1; Yee et al. 1996; Carlberg et al. 1996) and comprise the brightest clusters in the *Einstein*

Observatory Extended Medium Sensitivity Survey (EMSS; Gioia et al. 1990).

To improve the statistics, this initial sample was augmented with an additional 30 clusters (listed in Table 1) that were observed using Megacam on CFHT in the g' and r' -band. To ensure a significant detection of the lensing signal, clusters with an ASCA temperature of $k_B T_X > 5$ keV, and redshifts $0.15 < z < 0.55$ were selected based on the results from Horner (2001). Note that 4 of the EMSS clusters studied by Hoekstra (2007) do not meet the X-ray temperature criterion¹. Finally Table 1 lists two additional clusters (Abell 222 and Abell 1234) that were located in the observed fields.

In this paper we therefore present weak lensing masses for 52 clusters of galaxies. The imaging data have been used in a number of related studies. For instance, the surface brightness profiles of the brightest cluster galaxies were studied in Bildfell et al. (2008). The CCCP sample also provided the high redshift subset in a study of the evolution of the dwarf-to-giant ratio by Bildfell et al. (2012).

The X-ray analysis is described in detail in Mahdavi et al. (2012) and the resulting X-ray luminosity and temperature as a function of redshift are presented in Figure 1 (top and middle panel, resp.), as well as the distribution of cluster redshifts (bottom panel). The sample is dominated by clusters at $z \sim 0.2$, with a tail out to $z \sim 0.5$. This mostly reflects the limitations of the input ASCA catalog. It is important to note, however, that no selection was made based on the optical properties or the dynamical state of the cluster. Interestingly, although the sample is by no means complete, Mahdavi et al. (2012) find that the X-ray properties appear to be representative. The statistics of the $L_X - T_X$ relation of the CCCP sample are indistinguishable from samples with well-characterized selection functions, such as MACS (Ebeling et al. 2010) and HIFLUGCS (Reiprich & Böhringer 2002).

For the clusters observed with Megacam and $z < 0.3$ the observations typically consist of four 400s exposures in g' and eight 600s exposures in r' . For the higher redshift clusters we obtained four 600s exposure in g' and twelve 600s exposures in r' . These integrations times enable us to use galaxies down to $r' = 25$ in our weak lensing analysis. We only use the r' data because they are deeper and have better image quality. The g' data are used to identify the cluster early-type galaxies, which lie on a well-defined color-magnitude relation. The exposure times and information about the data reduction of the clusters observed using the CFH12k camera in the B and R filters can be found in Hoekstra (2007).

2.1 Processing of optical imaging data

Current wide field imaging instruments such as MegaCam consist of a mosaic of chips, and special care needs to be taken to account for sudden jumps in the PSF properties when data from different exposures are combined. To avoid such problems altogether, the CCCP data are obtained in two sets of exposures. Each set of four (or six) exposures

is taken with small dithers. The two sets are offset by approximately half a chip in each direction to fill in most of the gaps between chips. Rather than combining all our data into a single deep frame, for our weak lensing analysis we consider each set separately and combine the measurements in the catalog stage.

The data were detrended using the Elixir pipeline developed at CFHT. The pipeline also provides photometric zeropoints and in most cases a reasonable first order astrometric solution. We verified that the data were indeed taken during photometric conditions. The astrometric solution provided by Elixir is not sufficiently accurate to combine the exposures into deeper images without affecting the PSF: errors in the astrometry lead to additional anisotropies in the images. Instead, we follow the procedure described in Hoekstra et al. (2006) to refine the astrometric solution. We use the USNO-A2 catalog to calibrate the red images from the Digital Sky Survey (POSS II), which in turn is used to generate a catalog of sources with accurate astrometric positions.

This new astrometric catalog is matched to each of the MegaCam images. Each set of exposures is then processed separately. We detect objects in each of the exposures and combine matched objects into a master catalog, which contains the average positions of the matched objects. This master catalog is used to derive the final second order astrometric solution for each chip. This step ensures that the objects in each set of exposures are accurately matched to the same position.

3 WEAK LENSING ANALYSIS

We briefly review the steps in the weak lensing analysis, but refer the reader to Hoekstra (2007) for a detailed discussion of the analysis and various issues that arise when interpreting the data. The first step is to detect the faint galaxies and identify the stars. The stars are used to correct the galaxy shapes for the effects of PSF anisotropy and seeing. To do so, we use the procedure developed by Kaiser et al. (1995) and Luppino & Kaiser (1997). Modifications to the original approach are described in Hoekstra et al. (1998) and Hoekstra et al. (2000). The same analysis pipeline was also used for the cosmic shear analysis presented in Hoekstra et al. (2006). Furthermore, the method also performed well in the Shear Testing Programme (Heymans et al. 2006; Massey et al. 2007), which demonstrated that we can recover the weak lensing signal with an accuracy of $\sim 2\%$.

As mentioned earlier, each set of stacked images is analysed separately. Because the images were taken with small offsets, we can analyse the data on a chip-by-chip basis. We thus obtain two catalogs for each cluster of galaxies. The two catalogs are merged and the measurements for the objects that appear in both are combined. The resulting catalog is used to derive the cluster masses presented below. However, the redundancy in the data allow us also to check for consistency of the lensing signal.

To quantify the lensing signal we consider the azimuthally averaged tangential shear $\langle \gamma_T \rangle$ as a function of distance r from the cluster centre (for which we use the positions listed in Table 1; also see §3.1). To minimize the

¹ These are MS1224.7+2007, MS1231.3+1542, MS1455.0+2232 and MS1512.4+3647.

Table 1. Basic information of the Canadian Cluster Comparison Project sample

(1)	(2)	(3)	(4)	(5)	(6)	(7)	(8)	(9)
	name	z	RA (J2000.0)	DEC (J2000.0)	offset [h_{70}^{-1} kpc]	mag	$\langle\beta\rangle$	$\langle\beta^2\rangle$
1	Abell 68	0.255	00 ^h 37 ^m 06.9 ^s	+09°09′24″	12	21-25	0.50	0.26
2	Abell 209	0.206	01 ^h 31 ^m 52.5 ^s	−13°36′40″	49	21-25	0.63	0.39
3	Abell 267	0.230	01 ^h 52 ^m 42.0 ^s	+01°00′26″	85	20-25	0.52	0.28
4	Abell 370	0.375	02 ^h 39 ^m 52.7 ^s	−01°34′18″	93	22-25	0.41	0.17
5	Abell 383	0.187	02 ^h 48 ^m 03.4 ^s	−03°31′44″	4	21-24.5	0.64	0.41
6	Abell 963	0.206	10 ^h 17 ^m 03.8 ^s	+39°02′51″	5	21-25	0.59	0.35
7	Abell 1689	0.183	13 ^h 11 ^m 30.0 ^s	−01°20′30″	6	21-24.5	0.64	0.41
8	Abell 1763	0.223	13 ^h 35 ^m 20.1 ^s	+41°00′04″	84	21-25	0.57	0.33
9	Abell 2218	0.176	16 ^h 35 ^m 48.8 ^s	+66°12′51″	36	21-24.5	0.64	0.42
10	Abell 2219	0.226	16 ^h 40 ^m 19.9 ^s	+46°42′41″	26	21-25	0.56	0.32
11	Abell 2390	0.228	21 ^h 53 ^m 36.8 ^s	+17°41′44″	2	21-25	0.59	0.34
12	MS 0015.9+1609	0.547	00 ^h 18 ^m 33.5 ^s	+16°26′16″	50	22-25.5	0.27	0.07
13	MS 0906.5+1110	0.170	09 ^h 09 ^m 12.6 ^s	+10°58′28″	2	21-25	0.67	0.46
14	MS 1224.7+2007	0.326	12 ^h 27 ^m 13.5 ^s	+19°50′56″	−	21-25	0.44	0.20
15	MS 1231.3+1542	0.235	12 ^h 33 ^m 55.4 ^s	+15°25′58″	22	21-25.5	0.58	0.34
16	MS 1358.4+6245	0.329	13 ^h 59 ^m 50.6 ^s	+62°31′05″	2	21-25	0.45	0.20
17	MS 1455.0+2232	0.257	14 ^h 57 ^m 15.1 ^s	+22°20′35″	7	21-25.5	0.56	0.32
18	MS 1512.4+3647	0.373	15 ^h 14 ^m 22.5 ^s	+36°36′21″	3	21-25.5	0.43	0.19
19	MS 1621.5+2640	0.428	16 ^h 23 ^m 35.5 ^s	+26°34′14″	54	21-25.5	0.37	0.14
20	CL0024.0+1652	0.390	00 ^h 26 ^m 35.6 ^s	+17°09′44″	25	22-25.5	0.38	0.14
21	Abell 115N	0.197	00 ^h 55 ^m 50.6 ^s	+26°24′38″	11	20-25	0.61	0.38
	Abell 115S	0.197	00 ^h 56 ^m 00.3 ^s	+26°20′33″	9	20-25	0.61	0.38
22	Abell 222	0.213	01 ^h 37 ^m 34.0 ^s	−12°59′29″	14	20-25	0.58	0.35
23	Abell 223N	0.207	01 ^h 38 ^m 02.3 ^s	−12°45′20″	−	20-25	0.59	0.36
	Abell 223S	0.207	01 ^h 37 ^m 56.0 ^s	−12°49′10″	10	20-25	0.59	0.36
24	Abell 520	0.199	04 ^h 54 ^m 10.1 ^s	+02°55′18″	430 ^a	20-25	0.61	0.38
25	Abell 521	0.253	04 ^h 54 ^m 06.9 ^s	−10°13′25″	47	21-25	0.53	0.29
26	Abell 586	0.171	07 ^h 32 ^m 20.3 ^s	+31°38′01″	14	20-25	0.63	0.40
27	Abell 611	0.288	08 ^h 00 ^m 56.8 ^s	+36°03′24″	12	21-25	0.48	0.24
28	Abell 697	0.282	08 ^h 42 ^m 57.6 ^s	+36°21′59″	20	21-25	0.50	0.26
29	Abell 851	0.407	09 ^h 42 ^m 57.5 ^s	+46°58′50″	231 ^a	22-25	0.38	0.15
30	Abell 959	0.286	10 ^h 17 ^m 36.0 ^s	+59°34′02″	39	21-25	0.50	0.26
31	Abell 1234	0.166	11 ^h 22 ^m 30.0 ^s	+21°24′22″	−	20-25	0.66	0.45
32	Abell 1246	0.190	11 ^h 23 ^m 58.8 ^s	+21°28′50″	−	20-25	0.62	0.40
33	Abell 1758E	0.279	13 ^h 32 ^m 38.4 ^s	+50°33′36″	318	21-25	0.52	0.27
	Abell 1758W	0.279	13 ^h 32 ^m 52.1 ^s	+50°31′34″	56	21-25	0.52	0.27
34	Abell 1835	0.253	14 ^h 01 ^m 02.1 ^s	+02°52′43″	12	21-25	0.53	0.29
35	Abell 1914	0.171	14 ^h 26 ^m 02.8 ^s	+37°49′28″	227 ^a	20-25	0.66	0.44
36	Abell 1942	0.224	14 ^h 38 ^m 21.9 ^s	+03°40′13″	0.7	20-25	0.58	0.34
37	Abell 2104	0.153	15 ^h 40 ^m 07.9 ^s	−03°18′16″	10	20-25	0.68	0.47
38	Abell 2111	0.229	15 ^h 39 ^m 40.5 ^s	+34°25′27″	108	20-25	0.57	0.33
39	Abell 2163	0.203	16 ^h 15 ^m 49.0 ^s	−06°08′41″	11	20-25	0.60	0.36
40	Abell 2204	0.152	16 ^h 32 ^m 47.0 ^s	+05°34′33″	4	20-25	0.68	0.46
41	Abell 2259	0.164	17 ^h 20 ^m 09.7 ^s	+27°40′08″	75	20-25	0.65	0.44
42	Abell 2261	0.224	17 ^h 22 ^m 27.2 ^s	+32°07′58″	5	20-25	0.57	0.33
43	Abell 2537	0.295	23 ^h 08 ^m 22.2 ^s	−02°11′32″	8	21-25	0.49	0.24
44	MS0440.5+0204	0.190	04 ^h 43 ^m 09.9 ^s	+02°10′19″	4	20-25	0.60	0.37
45	MS0451.6-0305	0.550	04 ^h 54 ^m 10.8 ^s	−03°00′51″	34	22-25	0.28	0.08
46	MS1008.1-1224	0.301	10 ^h 10 ^m 32.3 ^s	−12°39′53″	12	21-25	0.47	0.23
47	RXJ1347.5-1145	0.451	13 ^h 47 ^m 30.1 ^s	−11°45′09″	7	22-25	0.34	0.12
48	RXJ1524.6+0957	0.516	15 ^h 24 ^m 41.6 ^s	+09°59′34″	44	22-25	0.30	0.09
49	MACS J0717.5+3745	0.548	07 ^h 17 ^m 30.4 ^s	+37°45′38″	113	22-25	0.27	0.07
50	MACS J0913.7+4056	0.442	09 ^h 13 ^m 45.5 ^s	+40°56′29″	1	22-25	0.36	0.13
51	CIZA J1938+54	0.260	19 ^h 38 ^m 18.1 ^s	+54°09′40″	−	21-25	0.52	0.27
52	3C295	0.460	14 ^h 11 ^m 20.6 ^s	+52°12′10″	5	22-25	0.34	0.12

Column 2: cluster name; Column 3: cluster redshift; Column 4,5: right ascension and declination (J2000.0) of the adopted cluster center. In all but three cases (Abell 520, Abell 851 and Abell 1914) we take this to be the position of the brightest cluster galaxy (BCG). Column 6: the offset between the peak in the X-ray emission and the position of the BCG. For the values marked ^a we actually use the X-ray position as the cluster center. Note that not all clusters have modern X-ray data; Column 7: magnitude range used for the source galaxies. For clusters 1 – 20 this is the R_C filter and r' for the remaining clusters; Column 8,9: the average values of $\beta = D_{ls}/D_s$ and $\langle\beta^2\rangle$ (as explained in the text)

effect of the gaps between the chips we only consider the signal between $0.5 - 2h_{70}^{-1}\text{Mpc}$ and fit a singular isothermal sphere model:

$$\langle\gamma_T\rangle = \frac{r_E}{2r}, \quad (1)$$

where r_E is the Einstein radius. Under the assumption of isotropic orbits and spherical symmetry, the Einstein radius (in radians) is related to the line-of-sight velocity dispersion σ through

$$r_E = 4\pi \left(\frac{\sigma}{c}\right)^2 \langle\beta\rangle, \quad (2)$$

where $\langle\beta\rangle = \langle D_{ls}/D_s\rangle$ is the average ratio of the angular diameter distances between the lens and the source, and the observer and the source. The value of $\langle\beta\rangle$ depends on the source redshift distribution, and is discussed in detail in the following section. For our comparison we do need to account for small variations in the actual source redshift distribution because the two images may have different seeing. This is particularly true for pointings that were observed a year apart. We therefore follow the procedure described below and also determine average values for β for each pointing.

Figure 2 shows the results of our comparison: the independent measurements of the lensing signal for each cluster agree very well. For the difference in r_E between the two positions we find $\langle\Delta r_E\rangle = 0.07 \pm 0.37$. The reduced $\chi^2 = 0.51$, which is too small if the two measurements would have been uncorrelated. However, the uncertainty in r_E is determined by the error in the shape measurements, which is a combination of the noise in the image and the intrinsic shapes of the source galaxies. The latter will cause the measurements to be correlated and we need to account for this in the comparison. We find that due to gaps between the chips, masks, etc. $\sim 70\%$ of the objects appear in both catalogs within the aperture we use to fit the model. We estimate the expected variation in the difference in r_E by simulating the effect of image noise and shape noise from objects that appear in only one of the catalogs. We find that the random error is approximately 70% of the total (formal) error and we expect a reduced $\chi^2 \sim 0.5$, which is in good agreement with the actual value. This suggests that the results obtained for the two positions are indeed in good agreement with one another.

3.1 Choice of cluster center

To quantify the lensing signal we need to define the cluster center. If the adopted center is offset from the ‘true’ center the tangential shear is lowered and the inferred mass is also biased low. Hence, one option is to determine the location that maximizes the lensing signal, for instance by reconstructing the projected mass distribution (e.g., Kaiser & Squires 1993), or fitting a model to the data. Such an approach, however, will lead to masses that are biased high. Instead we (typically) choose the location of the brightest cluster galaxy (BCG) to define the cluster center.

The adopted centers are listed in Table 1. The projected offset between the location of the BCG and the peak of the X-ray emission determined by Mahdavi et al. (2012) are also listed. The distribution of offsets is presented in Figure 3. With the exception of the four clusters discussed below, the

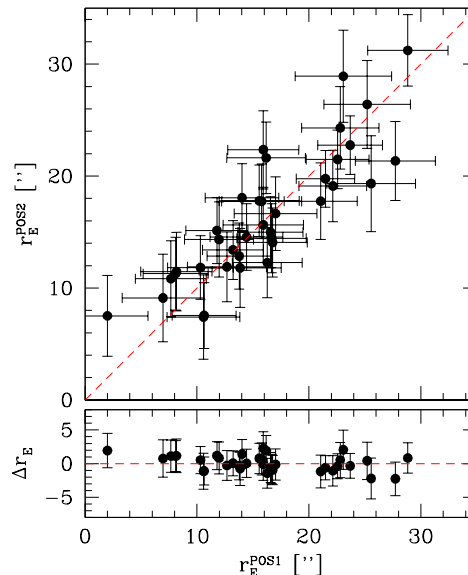


Figure 2. *top panel:* Plot of the best fit Einstein radii for the two sets of exposures. We have accounted for the small differences in the value for β for the two sets. *bottom panel:* Residuals from the one-to-one relation between Einstein radii. The lensing signals inferred from both data sets agree very well and the observed scatter agrees well with the expected variation.

offsets are less than $\sim 100\text{kpc}$, resulting in negligible biases in the cluster masses (see Figure 3 and discussion in §4.2). In three cases we use the position of the peak of the X-ray emission. Abell 520 is a well known merging system, and possibly the result of a three-way merger (Mahdavi et al. 2007; Okabe & Umetsu 2008; Jee et al. 2012). The unrelaxed cluster Abell 851 lacks a well defined brightest cluster galaxy and the X-ray emission peaks away from the concentration of bright cluster members. The BCG in Abell 1914 also shows a large offset from the peak in the X-ray emission. It is believed to be an ongoing merger (Dahle et al. 2002; Jones et al. 2005; Okabe & Umetsu 2008), showing high brightness tidal features (Feldmeier et al. 2004) and a radio halo (Giovannini et al. 1999; Kempner & Sarazin 2001). Abell 1758 is also a merging system with two peaks in the X-ray emission (David & Kempner 2004; Ragozzine et al. 2012). One peak is well centred on one of the BCGs, whereas the other component is clearly offset from the other BCG, which we nonetheless adopt as the center of the other cluster.

3.2 Source redshift distribution

To relate the lensing signal to physical quantities, such as mass, requires knowledge of the redshifts of the faint source galaxies. The higher the source redshift, the higher the lensing signal for a given mass. The redshifts need not be known with high precision, and photometric redshifts are sufficient. We lack the color information to derive photometric redshifts for our sources, but fortunately it suffices to assume an average redshift distribution that can be obtained from other data sets. This does lead to an increase in the uncer-

tainty with which the cluster mass can be determined. As shown in Hoekstra et al. (2011a) this contribution is small for clusters with $z \sim 0.2$, and only becomes relevant when studying high redshift clusters ($z > 0.6$).

We therefore can use the photometric redshifts from Ilbert et al. (2006) which are based on the CFHT Legacy Survey Deep fields and well matched in depth to what we need. Importantly, the survey covers a sufficiently large area of sky (4 fields of one square degree each) that sample variance, which has plagued earlier studies, is no longer important.

The use of photometric redshifts naturally accounts for galaxies in front of the cluster, which do not contribute to the lensing signal. However, the regions around clusters show large enhancements of galaxies (after all, that is what clusters of galaxies are) and many of those will end up in our catalog of sources. Our data only allow us to remove galaxies on the red-sequence. For our choice of filters, this only leads to a modest reduction in the level of contamination, because most faint cluster members are in fact blue.

The level of contamination after removing galaxies on the red-sequence depends on the choice of filter. For instance, Okabe et al. (2010a) find that their V and i' data allows for a relatively clean selection of sources. As discussed below, compared to our Megacam observations, the contamination is also lower for the clusters studied in Hoekstra (2007), which are based on B and R_C data. Hence our combination of g' and r' is not ideal. As shown in High et al. (2012), an efficient way to remove cluster members for our sample would be to obtain additional i' data. We lack such data and therefore we follow Hoekstra (2007) and derive an average correction for each cluster, by measuring the excess of source galaxies as a function of radius. We assume that the excess declines as $f_{cg}(r) \propto r^{-1}$, which is a reasonable description of the observed excess counts (c.f. Figure 3 in Hoekstra 2007). Note that we do exclude the galaxies on the red-sequence. To correct for the contamination by cluster members, the observed tangential shear is then scaled by a factor $1 + f_{cg}(r)$.

The correction leads to a $\sim 13\%$ increase in the best fit Einstein radii for the Megacam data, but only a $\sim 4\%$ increase for the CFH12k data. For the aperture masses the correction depends on the overdensity. We find that on average the results for M_{2500} are boosted by ~ 18 and $\sim 6\%$ for the Megacam and CFH12k data, respectively. The contamination is less important for M_{500} , which is based on measurements at larger radii: the masses based on the Megacam data are on average increased by $\sim 8\%$, whereas the masses of the other clusters are boosted by only $\sim 3\%$.

4 MASS DETERMINATION

One of the advantages of weak gravitational lensing is that it provides a direct measure of the projected mass distribution, without having to make assumptions about the density profile. In practice, however, the conversion of the observations into useful mass estimates does depend on the density profile, although the dependence can be weak. Furthermore, projected masses cannot be compared directly to results from other techniques, such as X-ray observations. Alternatively one can assume a parametric form for the den-

sity distribution and fit the predicted tangential distortion to the data. We discuss and compare the results from both approaches in the following sections.

4.1 Parametric mass model

Numerical simulations of cold dark matter indicate that the density profiles of dark matter halos are well described by the fitting function proposed by Navarro et al. (1996, 1997). The profile is characterized by two parameters: the mass of the halo and the concentration c (or characteristic scale). A commonly used method to infer cluster masses is to compare this model to the observed lensing signal and to determine the best fit values for the mass and the concentration, although c is typically poorly constrained. In simulations, however, the mass and the concentration are found to be correlated, albeit with an intrinsic scatter, which reflects the variation in halo formation histories. We follow the definitions of Hoekstra (2007), but use a more recent relation between the virial mass M_{vir} and concentration c , which was determined by Duffy et al. (2008) based on the cosmological parameters that best fit the WMAP5 observations (Komatsu et al. 2009):

$$c = 7.85 \left(\frac{M_{\text{vir}}^{\text{NFW}}}{2 \times 10^{12}} \right)^{-0.081} (1+z)^{-0.71}. \quad (3)$$

This relation is used when we fit the NFW model to the lensing signal at radii $0.5 - 2h_{70}^{-1}$ Mpc. The resulting values for $M_{\text{vir}}^{\text{NFW}}$ are presented in Table 2. For reference, we also list the values for M_{2500}^{NFW} and M_{500}^{NFW} , which are the masses within the radii where the mean mass density of the halo is respectively 2500 and 500 times the critical density at the redshift of the cluster, computed from the best fit virial mass (and Eqn. 3). We also fit a SIS model to the shear at these radii. The resulting Einstein radii and corresponding velocity dispersions are also listed in Table 2.

For the model fit, we avoid both the small and large radii. As discussed in Hoekstra (2001, 2003); Hoekstra et al. (2011b); Becker & Kravtsov (2011) structures along the line-of-sight contribute noise to the mass measurement. This 'cosmic noise' dominates at large radii, where the cluster signal is small. We account for the noise introduced by large-scale structure in the error budget. We do not fit the small scales in order to reduce (residual) contamination by cluster members and the effects of substructure (i.e., deviations from the simple NFW profile). Generally, the presence of substructure in the cluster core causes a reduction in the tangential shear, which biases the masses low (Hoekstra et al. 2002). As discussed in §3.1, the choice of cluster center is also important, as an offset from the true centre biases the mass low as well (also see Fig. 3). The bias is smaller if the offsets are small relative to the scales on which the shear is measured (see Figure 4 in Hoekstra et al. 2011a).

4.2 Deprojected aperture mass

Rather than adopting a parameterized model that is fit to the data, a unique feature of weak lensing is that the observed shear can be related directly to a density contrast. In essence, it allows us to infer the projected mass within an

Table 2. Canadian Cluster Comparison Project sample

(1)	(2)	(3)	(4)	(5)	(6)	(7)	(8)	(9)	(10)	(11)
name	r_E [arcsec]	σ [km/s]	$M_{0.5}^{\text{proj}}$	r_{2500} [h_{70}^{-1} kpc]	M_{2500}^{ap}	r_{500} [h_{70}^{-1} kpc]	M_{500}^{ap}	$M_{\text{vir}}^{\text{NFW}}$	M_{2500}^{NFW}	M_{500}^{NFW}
Abell 68	17.5 ± 2.6	1098^{+74}_{-80}	4.0 ± 0.6	520^{+32}_{-33}	$2.6^{+0.6}_{-0.5}$	1178^{+95}_{-87}	$6.0^{+1.9}_{-1.6}$	$13.6^{+3.4}_{-3.0}$	$2.7^{+0.7}_{-0.6}$	$7.5^{+1.9}_{-1.7}$
Abell 209	15.9 ± 2.8	937^{+76}_{-82}	3.2 ± 0.5	477^{+26}_{-31}	$1.9^{+0.4}_{-0.4}$	1254^{+65}_{-69}	$6.9^{+1.5}_{-1.5}$	$8.9^{+2.4}_{-2.2}$	$1.8^{+0.5}_{-0.5}$	$5.0^{+1.3}_{-1.2}$
Abell 267	14.8 ± 2.8	990^{+86}_{-94}	3.5 ± 0.6	489^{+26}_{-26}	$2.1^{+0.4}_{-0.4}$	1144^{+94}_{-89}	$5.4^{+1.7}_{-1.5}$	$9.7^{+2.8}_{-2.8}$	$2.0^{+0.6}_{-0.6}$	$5.4^{+1.5}_{-1.5}$
Abell 370	21.4 ± 2.8	1342^{+80}_{-85}	5.8 ± 0.8	570^{+36}_{-32}	$3.9^{+0.8}_{-0.7}$	1453^{+59}_{-68}	$12.9^{+2.3}_{-2.4}$	$28.6^{+6.7}_{-6.0}$	$5.2^{+1.2}_{-1.1}$	$15.6^{+3.7}_{-3.3}$
Abell 383	11.0 ± 3.4	769^{+111}_{-128}	2.0 ± 0.6	351^{+64}_{-43}	$0.7^{+0.5}_{-0.3}$	1059^{+133}_{-140}	$4.1^{+1.9}_{-1.6}$	$4.3^{+2.0}_{-2.0}$	$0.9^{+0.4}_{-0.4}$	$2.4^{+1.1}_{-1.1}$
Abell 963	13.6 ± 2.6	893^{+85}_{-59}	2.4 ± 0.5	420^{+35}_{-39}	$1.3^{+0.4}_{-0.4}$	1020^{+94}_{-102}	$3.7^{+1.4}_{-1.3}$	$7.9^{+2.1}_{-2.3}$	$1.6^{+0.5}_{-0.5}$	$4.4^{+1.2}_{-1.3}$
Abell 1689	31.1 ± 3.0	1298^{+85}_{-61}	6.3 ± 0.6	659^{+25}_{-25}	$4.9^{+0.6}_{-0.6}$	1594^{+87}_{-91}	$13.9^{+2.6}_{-2.5}$	$26.4^{+4.7}_{-4.3}$	$4.9^{+0.9}_{-0.8}$	$14.1^{+2.5}_{-2.3}$
Abell 1763	19.2 ± 2.9	1075^{+77}_{-82}	4.4 ± 0.5	554^{+27}_{-29}	$3.0^{+0.5}_{-0.5}$	1422^{+104}_{-104}	$10.2^{+2.7}_{-2.4}$	$13.6^{+3.3}_{-3.3}$	$2.7^{+0.6}_{-0.6}$	$7.5^{+1.8}_{-1.8}$
Abell 2218	19.5 ± 3.1	1024^{+76}_{-82}	3.6 ± 0.6	524^{+38}_{-40}	$2.4^{+0.6}_{-0.6}$	1155^{+81}_{-80}	$5.2^{+1.4}_{-1.3}$	$11.8^{+3.1}_{-2.9}$	$2.4^{+0.6}_{-0.6}$	$6.5^{+1.7}_{-1.6}$
Abell 2219	18.5 ± 2.7	1067^{+70}_{-75}	4.2 ± 0.6	545^{+32}_{-40}	$2.9^{+0.6}_{-0.6}$	1374^{+76}_{-75}	$9.3^{+2.0}_{-1.9}$	$14.3^{+3.4}_{-3.0}$	$2.8^{+0.7}_{-0.6}$	$7.8^{+1.9}_{-1.6}$
Abell 2390	23.2 ± 2.6	1171^{+61}_{-64}	4.3 ± 0.5	555^{+24}_{-26}	$3.1^{+0.5}_{-0.5}$	1345^{+62}_{-61}	$8.7^{+1.7}_{-1.6}$	$20.7^{+3.7}_{-3.6}$	$3.9^{+0.7}_{-0.7}$	$11.2^{+2.0}_{-1.9}$
MS 0015.9+1609	14.1 ± 2.7	1356^{+118}_{-129}	6.6 ± 0.8	567^{+34}_{-35}	$4.7^{+0.9}_{-0.9}$	1626^{+59}_{-76}	$22.2^{+3.9}_{-4.0}$	$26.8^{+8.5}_{-7.5}$	$4.8^{+1.5}_{-1.5}$	$14.8^{+4.7}_{-4.1}$
MS 0906.5+1110	16.0 ± 2.8	906^{+73}_{-79}	3.0 ± 0.5	477^{+32}_{-25}	$1.8^{+0.4}_{-0.4}$	1380^{+98}_{-98}	$8.9^{+2.0}_{-2.0}$	$9.3^{+2.4}_{-2.3}$	$1.9^{+0.5}_{-0.5}$	$5.1^{+1.3}_{-1.3}$
MS 1224.7+2007	8.6 ± 2.8	817^{+121}_{-141}	2.5 ± 0.7	388^{+77}_{-77}	$1.2^{+0.5}_{-0.6}$	881^{+77}_{-72}	$2.7^{+1.1}_{-1.0}$	$4.7^{+2.5}_{-2.1}$	$1.0^{+0.5}_{-0.4}$	$2.7^{+1.4}_{-1.2}$
MS 1231.3+1542	5.1 ± 2.6	549^{+118}_{-149}	0.8 ± 0.5	295^{+40}_{-44}	$0.5^{+0.2}_{-0.2}$	547^{+93}_{-125}	$0.6^{+0.5}_{-0.4}$	$1.4^{+1.3}_{-0.9}$	$0.3^{+0.3}_{-0.2}$	$0.8^{+0.8}_{-0.5}$
MS 1358.4+6245	12.8 ± 2.6	994^{+90}_{-99}	3.6 ± 0.6	471^{+27}_{-35}	$2.1^{+0.4}_{-0.5}$	1140^{+88}_{-85}	$5.9^{+1.9}_{-1.7}$	$10.7^{+3.4}_{-3.0}$	$2.1^{+0.7}_{-0.6}$	$6.0^{+1.9}_{-1.7}$
MS 1455.0+2232	14.6 ± 2.3	945^{+67}_{-72}	2.7 ± 0.5	423^{+32}_{-29}	$1.4^{+0.4}_{-0.3}$	1051^{+49}_{-61}	$4.3^{+1.2}_{-1.2}$	$8.6^{+1.9}_{-1.9}$	$1.8^{+0.4}_{-0.4}$	$4.8^{+1.0}_{-1.1}$
MS 1512.4+3647	7.7 ± 2.7	786^{+140}_{-140}	1.8 ± 0.7	326^{+40}_{-54}	$0.7^{+0.3}_{-0.3}$	859^{+153}_{-215}	$2.7^{+1.9}_{-1.7}$	$4.3^{+2.0}_{-2.0}$	$0.9^{+0.4}_{-0.4}$	$2.5^{+1.2}_{-1.2}$
MS 1621.5+2640	15.0 ± 2.7	1186^{+99}_{-108}	4.2 ± 0.7	476^{+49}_{-73}	$2.4^{+0.8}_{-1.0}$	1205^{+66}_{-73}	$7.8^{+2.0}_{-2.0}$	$16.8^{+5.1}_{-4.5}$	$3.2^{+1.0}_{-0.9}$	$9.4^{+2.8}_{-2.5}$
CL0024.0+1652	16.9 ± 3.0	1242^{+101}_{-110}	5.2 ± 0.8	545^{+30}_{-38}	$3.5^{+0.7}_{-0.7}$	1323^{+95}_{-111}	$9.9^{+2.8}_{-2.8}$	$20.4^{+6.1}_{-5.5}$	$3.8^{+1.1}_{-1.0}$	$11.2^{+3.3}_{-3.0}$
Abell 115N	11.9 ± 2.8	814^{+88}_{-98}	1.7 ± 0.5	332^{+55}_{-87}	$0.6^{+0.4}_{-0.4}$	1041^{+99}_{-143}	$3.9^{+1.4}_{-1.5}$	$5.7^{+1.7}_{-1.9}$	$1.2^{+0.4}_{-0.4}$	$3.2^{+1.0}_{-1.0}$
Abell 115S	12.0 ± 2.8	819^{+85}_{-95}	2.4 ± 0.5	355^{+82}_{-43}	$0.8^{+0.7}_{-0.3}$	1157^{+71}_{-72}	$5.4^{+1.3}_{-1.2}$	$6.8^{+2.1}_{-1.9}$	$1.4^{+0.4}_{-0.4}$	$3.8^{+1.1}_{-1.2}$
Abell 222	15.1 ± 2.9	934^{+82}_{-90}	3.0 ± 0.5	451^{+45}_{-54}	$1.6^{+0.6}_{-0.5}$	1181^{+68}_{-70}	$5.8^{+1.3}_{-1.2}$	$7.9^{+2.4}_{-2.1}$	$1.6^{+0.5}_{-0.4}$	$4.4^{+1.4}_{-1.2}$
Abell 223N	16.7 ± 2.9	976^{+78}_{-85}	3.0 ± 0.5	441^{+47}_{-57}	$1.5^{+0.5}_{-0.7}$	1235^{+83}_{-78}	$6.6^{+1.6}_{-1.4}$	$9.7^{+2.8}_{-2.4}$	$2.0^{+0.6}_{-0.5}$	$5.3^{+1.5}_{-1.3}$
Abell 223S	11.3 ± 3.0	805^{+96}_{-109}	2.5 ± 0.5	388^{+57}_{-56}	$1.0^{+0.5}_{-0.4}$	1261^{+107}_{-96}	$7.0^{+2.1}_{-1.7}$	$5.7^{+2.0}_{-2.1}$	$1.2^{+0.5}_{-0.5}$	$3.2^{+1.1}_{-1.2}$
Abell 520	20.4 ± 2.7	1064^{+66}_{-70}	3.4 ± 0.5	495^{+28}_{-31}	$2.1^{+0.4}_{-0.4}$	1176^{+72}_{-69}	$5.6^{+1.3}_{-1.2}$	$13.2^{+2.5}_{-2.8}$	$2.6^{+0.5}_{-0.6}$	$7.2^{+1.4}_{-1.5}$
Abell 521	11.8 ± 2.9	869^{+98}_{-110}	3.0 ± 0.5	420^{+57}_{-88}	$1.4^{+0.6}_{-0.7}$	1202^{+88}_{-75}	$6.4^{+1.7}_{-1.4}$	$8.6^{+2.6}_{-2.6}$	$1.8^{+0.5}_{-0.5}$	$4.8^{+1.4}_{-1.4}$
Abell 586	14.1 ± 3.2	868^{+92}_{-103}	2.5 ± 0.6	420^{+48}_{-49}	$1.3^{+0.5}_{-0.4}$	1192^{+91}_{-100}	$5.7^{+1.6}_{-1.5}$	$6.8^{+2.4}_{-2.2}$	$1.4^{+0.5}_{-0.5}$	$3.8^{+1.3}_{-1.2}$
Abell 611	12.8 ± 2.9	954^{+99}_{-110}	3.3 ± 0.7	459^{+44}_{-55}	$1.8^{+0.6}_{-0.6}$	1146^{+65}_{-62}	$5.8^{+1.3}_{-1.2}$	$8.2^{+2.8}_{-2.5}$	$1.7^{+0.6}_{-0.5}$	$4.6^{+1.6}_{-1.4}$
Abell 697	16.6 ± 2.7	1059^{+87}_{-87}	4.1 ± 0.5	518^{+32}_{-38}	$2.6^{+0.5}_{-0.5}$	1371^{+56}_{-49}	$9.8^{+1.5}_{-1.5}$	$11.4^{+2.7}_{-2.5}$	$2.3^{+0.5}_{-0.5}$	$6.4^{+1.5}_{-1.4}$
Abell 851	18.1 ± 3.0	1272^{+98}_{-105}	5.1 ± 0.5	522^{+18}_{-22}	$3.1^{+0.4}_{-0.4}$	1343^{+85}_{-88}	$10.6^{+2.5}_{-2.3}$	$20.0^{+5.4}_{-5.0}$	$3.8^{+1.0}_{-0.9}$	$11.1^{+3.0}_{-2.8}$
Abell 959	21.8 ± 2.9	1217^{+77}_{-82}	4.7 ± 0.6	554^{+29}_{-32}	$3.2^{+0.6}_{-0.6}$	1276^{+72}_{-71}	$7.9^{+1.7}_{-1.6}$	$18.6^{+4.0}_{-3.9}$	$3.6^{+0.8}_{-0.7}$	$10.2^{+2.2}_{-2.1}$
Abell 1234	17.3 ± 2.8	938^{+69}_{-74}	2.3 ± 0.5	423^{+29}_{-31}	$1.3^{+0.3}_{-0.3}$	980^{+96}_{-94}	$3.1^{+1.2}_{-1.0}$	$7.9^{+1.9}_{-2.0}$	$1.6^{+0.4}_{-0.4}$	$4.4^{+1.0}_{-1.1}$
Abell 1246	14.4 ± 2.6	880^{+71}_{-77}	2.5 ± 0.4	409^{+36}_{-43}	$1.2^{+0.4}_{-0.4}$	1080^{+53}_{-80}	$4.3^{+0.9}_{-1.1}$	$8.2^{+1.8}_{-1.9}$	$1.7^{+0.4}_{-0.4}$	$4.6^{+1.0}_{-1.0}$
Abell 1758E	17.1 ± 2.4	1062^{+68}_{-69}	4.2 ± 0.5	530^{+27}_{-31}	$2.8^{+0.5}_{-0.5}$	1391^{+92}_{-78}	$10.2^{+2.4}_{-1.9}$	$12.9^{+2.6}_{-2.6}$	$2.5^{+0.5}_{-0.5}$	$7.1^{+1.4}_{-1.4}$
Abell 1758W	21.0 ± 2.4	1175^{+70}_{-63}	4.1 ± 0.5	522^{+25}_{-29}	$2.7^{+0.4}_{-0.5}$	1388^{+52}_{-60}	$10.1^{+1.6}_{-1.6}$	$16.4^{+2.9}_{-2.9}$	$3.2^{+0.6}_{-0.6}$	$9.0^{+1.7}_{-1.6}$
Abell 1835	23.2 ± 2.9	1218^{+70}_{-74}	4.6 ± 0.5	560^{+25}_{-27}	$3.2^{+0.5}_{-0.5}$	1322^{+51}_{-52}	$8.5^{+1.4}_{-1.4}$	$18.9^{+3.8}_{-3.5}$	$3.6^{+0.7}_{-0.7}$	$10.3^{+2.1}_{-1.9}$
Abell 1914	21.7 ± 2.5	1057^{+55}_{-57}	3.5 ± 0.4	509^{+20}_{-21}	$2.2^{+0.3}_{-0.3}$	1193^{+55}_{-56}	$5.7^{+1.1}_{-1.1}$	$13.2^{+2.2}_{-2.1}$	$2.6^{+0.4}_{-0.4}$	$7.2^{+1.2}_{-1.1}$
Abell 1942	14.4 ± 2.6	916^{+75}_{-81}	3.1 ± 0.4	462^{+25}_{-25}	$1.8^{+0.3}_{-0.3}$	1070^{+61}_{-69}	$4.4^{+1.1}_{-1.0}$	$8.9^{+2.1}_{-1.9}$	$1.8^{+0.4}_{-0.4}$	$5.0^{+1.1}_{-1.1}$
Abell 2104	23.0 ± 3.6	1067^{+80}_{-86}	3.4 ± 0.5	513^{+34}_{-45}	$2.2^{+0.5}_{-0.6}$	1235^{+84}_{-80}	$6.2^{+1.6}_{-1.4}$	$13.2^{+3.5}_{-3.1}$	$2.6^{+0.7}_{-0.6}$	$7.2^{+1.9}_{-1.7}$
Abell 2111	16.0 ± 2.7	974^{+74}_{-79}	3.4 ± 0.5	489^{+28}_{-29}	$2.1^{+0.4}_{-0.4}$	1087^{+87}_{-87}	$4.6^{+1.7}_{-1.4}$	$9.7^{+1.9}_{-2.2}$	$2.0^{+0.4}_{-0.5}$	$5.4^{+1.1}_{-1.2}$
Abell 2163	21.2 ± 3.2	1094^{+80}_{-86}	4.2 ± 0.6	556^{+38}_{-42}	$3.0^{+0.7}_{-0.7}$	1403^{+109}_{-102}	$9.6^{+2.7}_{-2.2}$	$14.7^{+3.5}_{-3.4}$	$2.9^{+0.7}_{-0.7}$	$8.0^{+1.9}_{-1.8}$
Abell 2204	25.4 ± 3.1	1128^{+65}_{-69}	4.4 ± 0.5	583^{+29}_{-31}	$3.3^{+0.6}_{-0.6}$	1357^{+73}_{-70}	$8.3^{+1.6}_{-1.5}$	$15.7^{+3.0}_{-3.0}$	$3.1^{+0.6}_{-0.6}$	$8.5^{+1.6}_{-1.6}$
Abell 2259	13.3 ± 3.0	830^{+87}_{-97}	1.9 ± 0.5	348^{+43}_{-38}	$0.7^{+0.3}_{-0.2}$	1063^{+70}_{-120}	$4.0^{+1.1}_{-1.4}$	$6.1^{+2.2}_{-1.8}$	$1.3^{+0.5}_{-0.4}$	$3.4^{+1.2}_{-1.0}$
Abell 2261	22.2 ± 2.8	1153^{+69}_{-73}	5.0 ± 0.5	605^{+26}_{-28}	$3.9^{+0.6}_{-0.6}$	1540^{+54}_{-46}	$13.0^{+1.8}_{-1.6}$	$17.5^{+3.2}_{-3.2}$	$3.4^{+0.6}_{-0.6}$	$9.5^{+1.8}_{-1.8}$
Abell 2537	18.7 ± 2.8	1150^{+80}_{-86}	4.9 ± 0.5	557^{+24}_{-26}	$3.3^{+0.5}_{-0.5}$	1235^{+50}_{-50}	$7.3^{+1.3}_{-1.3}$	$16.8^{+3.8}_{-3.5}$	$3.2^{+0.7}_{-0.7}$	$9.2^{+2.1}_{-1.9}$
MS0440.5+0204	11.5 ± 3.2	798^{+103}_{-117}	2.5 ± 0.6	419^{+46}_{-53}	$1.3^{+0.5}_{-0.6}$	867^{+56}_{-56}	$2.2^{+0.7}_{-0.6}$	$3.9^{+1.8}_{-1.6}$	$0.9^{+0.4}_{-0.4}$	$2.2^{+1.0}_{-1.0}$
MS0451.6-0305	9.5 ± 3.1	1086^{+162}_{-188}	3.6 ± 0.8	412^{+41}_{-42}	$1.8^{+0.6}_{-0.5}$	964^{+91}_{-108}	$4.6^{+1.6}_{-1.6}$	$11.1^{+4.5}_{-4.5}$	$2.2^{+1.0}_{-0.9}$	$6.3^{+2.6}_{-2.2}$
MS1008.1-1224	18.4 ± 3.1	1155^{+93}_{-101}	3.5 ± 0.6	475^{+33}_{-35}	$2.1^{+0.5}_{-0.4}$	1080^{+41}_{-63}	$4.9^{+1.0}_{-1.1}$	$15.0^{+4.0}_{-3.7}$	$2.9^{+0.8}_{-0.7}$	$8.3^{+2.2}_{-2.1}$
RXJ1347.5-1145	16.1 ± 3.0	1271^{+111}_{-121}	4.8 ± 0.7	502^{+38}_{-40}	$2.9^{+0.7}_{-0.7}$	1270^{+100}_{-144}	$9.5^{+2.7}_{-3.1}$	$18.2^{+5.9}_{-5.1}$	$3.4^{+1.1}_{-1.0}$	$10.1^{+3.3}_{-2.8}$
RXJ1524.6+0957	7.3 ± 2.8	914^{+157}_{-189}	2.8 ± 0.9	344^{+59}_{-67}	$1.0^{+0.6}_{-0.3}$	883^{+112}_{-129}	$3.4^{+1.6}_{-1.4}$	$7.5^{+3.6}_{-3.4}$	$1.5^{+0.7}_{-0.7}$	$4.9^{+2.1}_{-1.9}$
MACS J0717.5+3745	21.1 ± 3.2	1648^{+117}_{-125}	7.2 ± 1.0	612^{+40}_{-51}	$5.9^{+1.3}_{-1.4}$	1483^{+74}_{-76}	$16.9^{+3.2}_{-3.0}$	$51.4^{+11.3}_{-10.8}$	$8.7^{+1.9}_{-1.8}$	$27.9^{+6.1}_{-5.9}$
MACS J0913.7+4056	9.8 ± 3.2	974								

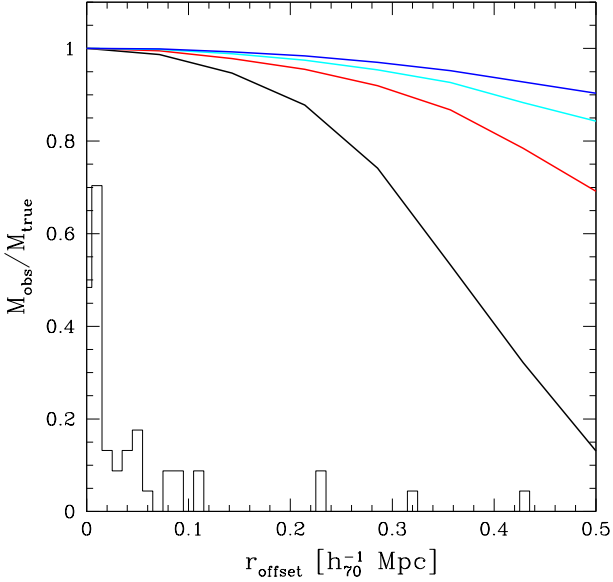


Figure 3. Plot of the ratio of the inferred lensing mass and the true mass as a function of centroid offset for an NFW halo with a virial mass $M = 5 \times 10^{14} M_{\odot}$. The lensing mass is inferred from the ζ_c statistic as explained in the text. The curves correspond to M_{2500} (lowest curve; black), M_{1000} (red), M_{500} (cyan) and M_{200} (highest curve; blue). For overdensities $\Delta < 1000$, the observed value for M_{Δ} is not very sensitive to centroiding errors because the large scale shear is not affected. The histogram shows the distribution of offsets between the BCG and the peak of the X-ray emission, suggesting that miscentering is a small effect for the CCCP sample.

aperture, with relatively few assumptions about the actual mass distribution. We use that (Clowe et al. 1998):

$$\zeta_c(r_1) = 2 \int_{r_1}^{r_2} d \ln r \langle \gamma_t \rangle + \frac{2r_{\max}^2}{r_{\max}^2 - r_2^2} \int_{r_2}^{r_{\max}} d \ln r \langle \gamma_t \rangle, \quad (4)$$

which can be expressed in terms of the mean dimensionless surface density interior to r_1 relative to the mean surface density in an annulus from r_2 to r_{\max}

$$\zeta_c(r_1) = \bar{\kappa}(r' < r_1) - \bar{\kappa}(r_2 < r' < r_{\max}). \quad (5)$$

This shows that we can determine the average surface density within a given aperture up to a constant (i.e., the mean convergence in the annulus). The surface density in the annulus cannot be ignored, even though it is small for the wide field imaging data used here. We estimate the mean surface density in the annulus based on the best fit NFW model. For the clusters observed with the CFH12k camera, we adopt $r_2 = 600''$ and $r_{\max} = 1000''$, and for the Megacam observations we use $r_2 = 900''$ and $r_{\max} = 1500''$ (reflecting the larger field-of-view).

Thanks to our ability to measure the lensing signal out to large radii, the (model dependent) correction to the mass is only $\sim 8\%$ for M_{500} and $\sim 3\%$ for M_{2500} . The correction is larger if we use the best fit SIS model instead of the best NFW fit. The difference is largest for M_{500} , which would increase by $\sim 10\%$ compared to the results listed in Table 2, whereas M_{2500} would increase by $\sim 4\%$ if we use

the SIS fit to estimate the convergence in the annulus. Note that Okabe et al. (2010a) assume that the contribution in the annulus can be ignored, which is definitely not the case, considering the bias it introduces for a large sample of clusters. Consequently we cannot compare our results directly to the aperture masses listed in Okabe et al. (2010a).

Although the NFW model should be a good description of the average mass distribution on small scales, it is less accurate on large scales because structures near the cluster will contribute to the lensing signal. This can be studied in the context of a halo-model (e.g. Johnston et al. 2007). However, for the radii and masses we study here this so-called two-halo contribution is expected to be small (Johnston et al. 2007; Becker & Kravtsov 2011).

We examined the effect of errors in the adopted cluster center on the inferred aperture masses. The results are presented in Figure 3 for four overdensities Δ . For higher overdensities one needs to integrate the shear signal to smaller radii and the mass becomes more sensitive to centroid offsets. However, the observed offsets between the BCG position and the peak of the X-ray emission suggest that the bias in our masses are negligible (even for M_{2500}). Note that for three of the four clusters with offsets larger than $200h_{70}^{-1}$ kpc we use the X-ray center instead (see §3.1)

To compare to results from other methods the aperture masses need to be deprojected, under the assumption of spherical symmetry. Non-parametric deprojections are noisy, and we therefore employ a different approach, which was also used in Hoekstra (2007). For each aperture we determine which NFW model would yield the observed projected mass. The corresponding mass of the model is then taken to be the deprojected mass. Hence we assume that the density profile along the line-of-sight is described by the NFW model. Note that each aperture is treated independently: the corresponding virial mass (and consequently the concentration given by Eqn. 3), is allowed to vary with radius. The resulting profiles are used to measure r_{Δ} . The results for $\Delta = 2500$ and 500 are listed in Table 2, along with the corresponding values for r_{Δ} .

Becker & Kravtsov (2011) have shown that fitting an NFW model to the observed lensing signal can lead to biased mass estimates when the mass and concentration are free parameters (also see Meneghetti et al. 2010; Bahé et al. 2012; High et al. 2012). Becker & Kravtsov (2011) also make the point that the bias is likely to depend on the method that was used to infer the mass, as well as the range in angular scales that is considered. In particular, they show that extending the NFW fits to large radii ($> 10'$) tends to bias the masses low by $\sim 6\%$. Most of the bias appears to be caused by the fact that the NFW fit overestimates the reduced tangential shear on scales of $10' - 20'$ before two-halo contributions (see e.g. Johnston et al. 2007) become important. The NFW fit results presented in Table 2 are based on the lensing signal at radii $0.5 - 2h_{70}^{-1}$ Mpc, for which the bias should be small.

The situation for the aperture masses is less clear. High et al. (2012) used simulations to find that their approach underestimates the masses at R_{500} by 6–13%. However, they use the ζ -statistic proposed by Fahlman et al. (1994), which requires an estimate of κ in an annulus ranging from R_{500} out to $16'$, which is the largest scale considered by High et al. (2012). Compared to our approach, the correc-

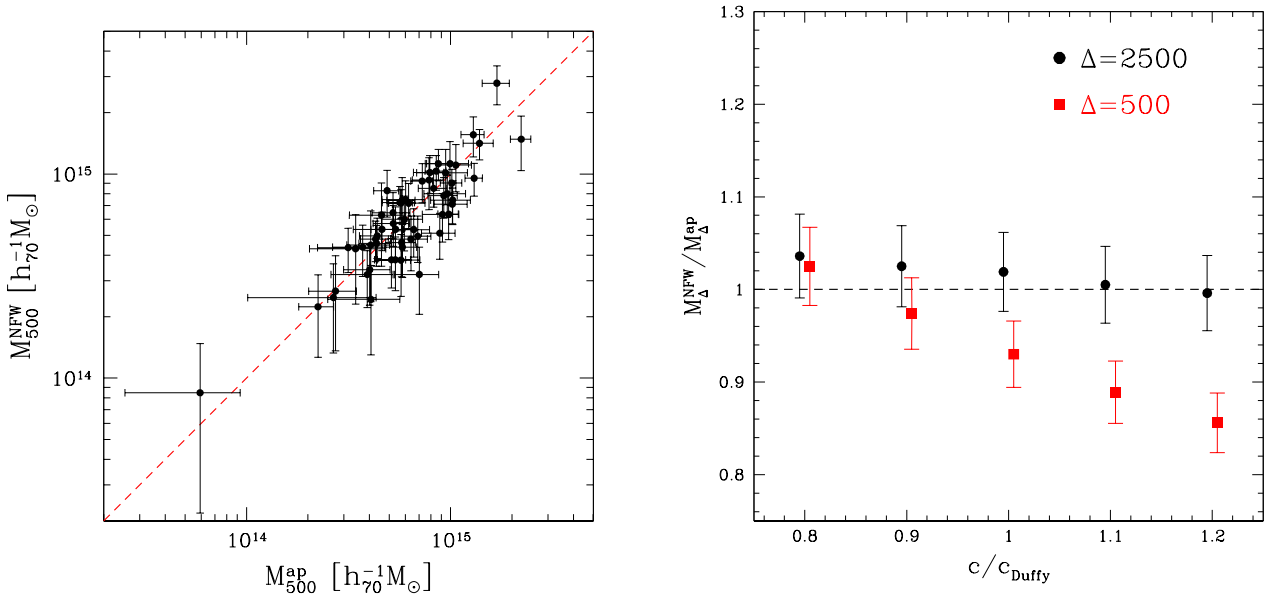


Figure 4. *left panel:* Value for M_{500} from the best fit NFW model to the lensing signal at radii $0.5 - 2h_{70}^{-1}$ Mpc versus the M_{500} inferred from the deprojected aperture mass. The mass-concentration relation from Duffy et al. (2008) was used for the NFW fit. The dashed red line indicates the line of equality. *right panel:* The average ratio of the best fit NFW mass and the deprojected aperture mass when the normalization of the mass-concentration (Equation 3) is changed. High normalisations lead to inconsistent estimates for M_{500} .

Table 3. Sensitivity to $c(M)$ normalization

Δ	aperture mass		NFW fit	
	$\alpha = 0.8$	$\alpha = 1.2$	$\alpha = 0.8$	$\alpha = 1.2$
2500	0.88 ± 0.03	1.09 ± 0.03	0.90 ± 0.03	1.07 ± 0.03
1000	0.92 ± 0.01	1.06 ± 0.01	1.00 ± 0.04	0.99 ± 0.03
500	0.94 ± 0.01	1.04 ± 0.01	1.06 ± 0.04	0.95 ± 0.03
vir	–	–	1.16 ± 0.05	0.89 ± 0.03

Table of the ratio $\langle M_{\Delta}(\alpha c_{\text{Duffy}}) / M_{\Delta}(c_{\text{Duffy}}) \rangle$ when the masses are estimated from deprojecting the aperture masses (Columns 2 & 3) or by fitting an NFW model to the data (Columns 4 & 5). The errors correspond to the standard deviation of the ratios.

tion for the convergence in this annulus is much larger, about 35% at R_{500} , and thus more sensitive to deviations from the assumed density profile. We expect the bias to be proportional to this correction, and consequently we expect any bias in our deprojected masses to be considerably smaller than those of High et al. (2012).

4.3 Sensitivity to mass-concentration relation

Both procedures we use to derive cluster masses depend on the adopted mass-concentration relation (Equation 3). It is important to note that $c(M)$ depends on the cosmology: the concentration is related to the mean density of the Universe when the cluster was formed (e.g. Navarro et al. 1996; Bullock et al. 2001). As more massive halos form later in a Λ CDM cosmology, they will have smaller concentrations (but see Prada et al. 2011). Furthermore, the mass depen-

dence is rather modest when considering a relatively small mass range, as is done here.

The amplitude, however, is sensitive to the matter density Ω_m and the normalization of the matter power spectrum σ_8 and various fitting functions have been published (e.g. Bullock et al. 2001; Neto et al. 2007; Macciò et al. 2008; Prada et al. 2011) in addition to Equation 3. The observed mass-concentration relation can therefore be used in principle to constrain cosmological parameters (Ettori et al. 2010). Note that the simulations studied by Prada et al. (2011) prefer a significantly higher normalization. This claim appears to be supported by a number of observational results (e.g. Zitrin et al. 2010, 2011; Umetsu et al. 2011). It is, however, not clear whether these findings are biased by the fact that many of these are well-known strong lensing clusters. For instance, accounting for the 3D structure of the clusters appears to yield lower concentrations (Morandi & Limousin 2012). An important complication, which requires further study, is the role of baryons, which have not been considered in these studies. The effect depends on the feedback model, with steeper profiles if radiative cooling is efficient, and shallower profiles if feedback is effective (e.g. Lewis et al. 2000; Duffy et al. 2010).

A detailed study of the mass-concentration relation is beyond the scope of this paper, but it is nonetheless useful to examine the sensitivity of our mass estimates to our choice for $c(M)$ by varying its normalization. We studied the average change in the deprojected aperture masses and the NFW fits and list the results in Table 3 for different overdensities. The deprojected mass converges to the projected mass for large radii and hence it is not surprising that the aperture mass values for M_{500} are the least sensitive, with a 20% variation only changing the masses by $\sim 5\%$. The NFW fits

show a similar variation for M_{500} but the dependence with c is opposite. Interestingly, the value for M_{1000}^{NFW} is nearly independent of the adopted normalization, suggesting that this provides the most robust mass estimate when fitting an NFW profile to the tangential shear profile between 0.5 and $2h_{70}^{-1}\text{Mpc}$.

If the density profiles are (on average) well described by the NFW profile we expect good agreement between our different approaches to measure the cluster masses. The left panel of Figure 4 shows the results when M_{500}^{NFW} from the NFW fit is compared to the deprojected aperture mass estimates M_{500}^{ap} . Note that the results are slightly correlated because the NFW fit uses data out to $2h_{70}^{-1}\text{Mpc}$, whereas the typical values for r_{500} are $\sim 1.2h_{70}^{-1}\text{Mpc}$. Hence there is some overlap in the shear signals that were used to derive the masses. We fit a linear relation to the masses and find that the ratio of NFW to deprojected aperture mass is 0.93 ± 0.04 .

The right panel of Figure 4 shows how this ratio varies with the normalization of the mass-concentration relation for both M_{2500} (black points) and M_{500} (red squares). We find that for $\Delta = 2500$ the agreement is good for a wide range of normalizations. The comparison of M_{500} suggests a preference for a lower concentration, but a more detailed analysis is needed before a conclusion can be drawn. For instance, the presence of substructure biases the NFW masses low. However, significantly larger concentrations, such as found by Prada et al. (2011) lead to inconsistent mass estimates, and thus are at odds with our results.

5 SZE SCALING RELATION

On sufficiently large scales, clusters can be considered representative reservoirs of baryons and dark matter. We therefore expect correlations between the observable properties and the underlying mass: more massive systems should have more of everything. These so-called scaling relations are the result of the physical processes that give rise to the formation and evolution of galaxy clusters. If gravity is the dominant process, the scaling relations and their evolution can be predicted (Kaiser 1986). These self-similar models predict simple power law scaling relations between the baryonic tracers and the cluster mass.

Additional non-gravitational processes, such as AGN feedback can in principle lead to significant deviations from the simple single power law model (e.g., Babul et al. 2002; McCarthy et al. 2004). Gravity is, however, expected to be the dominant process for the masses probed by CCCP. Furthermore the mass range we study here is limited and we therefore assume that the scaling relation between the lensing mass M_{WL} and mass proxy M_{proxy} , in our case the Sunyaev-Zel'dovich effect (SZE) signal, can be described by a single power law:

$$M_{\text{WL}} = E(z)^\gamma M_0 \left(\frac{M_{\text{proxy}}}{M_{\text{pivot}}} \right)^\alpha, \quad (6)$$

where M_0 is the normalisation, M_{pivot} is the pivot point, α the power law slope and $E(z) = H(z)/H_0$ is the normalized Hubble parameter. If we fit Eqn. 6 to the measurements in §5.1 the resulting χ^2 values are larger than expected, suggesting the presence of intrinsic scatter (also see

Mahdavi et al. 2012, for a comparison to the X-ray properties). It is important to account for the intrinsic scatter when fitting a scaling relation to the data, because ignoring the scatter will generally bias the best fit parameters. The presence of intrinsic scatter is also relevant when assessing the performance of mass-proxies: an observable with larger statistical errors but smaller intrinsic scatter may be preferable over one with small statistical errors but a large intrinsic scatter.

Some of this scatter arises from the fact that the lensing signal measures the projected mass along the line-of-sight, whereas for instance the X-ray luminosity probes the virialized regions of the cluster. Hence, the lensing mass is more sensitive to the fact that dark matter halos are triaxial. The separation of this ‘geometric’ source of scatter from the physical scatter requires a careful comparison with numerical simulations, incorporating in detail the steps taken in the analysis of the observations. The effects of triaxiality on weak lensing mass measurements have been studied using numerical simulations (e.g., Metzler et al. 2001; Meneghetti et al. 2010; Becker & Kravtsov 2011) and analytically (Corless & King 2007). The studies by Corless & King (2007) and Meneghetti et al. (2010) suggest a contribution of $\sigma_M \sim 0.15M_{\text{WL}}$ due to the triaxiality of the cluster dark matter halo.

5.1 Fitting procedure

We fit scaling relations to the actual measurements (not the logarithm), because they follow a (close to) normal distribution, even if the relative error is large. The intrinsic scatter, however, is assumed to be log-normal, but relatively small. It can therefore be approximated by a normal distribution with a dispersion $\sigma_Q \approx \ln(10)Q\sigma_{\log Q}$ (we use the log with base 10).

A number of techniques exist to fit a model to data with errors in both directions, but we follow a maximum likelihood approach (also see Weiner et al. (2006) for a detailed discussion). For a model f with parameters \mathbf{a} , the predicted values are $y_i = f(x_i; \mathbf{a})$. The uncertainties in x_i and y_i are given by $\sigma_{x,i}$ and $\sigma_{y,i}$. If we assume a Gaussian intrinsic scatter σ_Q in the y coordinate, the likelihood \mathcal{L} is given by

$$\mathcal{L} = \prod_{i=1}^n \frac{1}{\sqrt{2\pi}w_i} \exp \left[-\frac{[y_i - f(x_i; \mathbf{a})]^2}{2w_i^2} \right], \quad (7)$$

where w_i accounts for the scatter:

$$w_i^2 = \left[\frac{df}{dx}(x_i) \right]^2 \sigma_{x,i}^2 + \sigma_{y,i}^2 + \sigma_Q^2. \quad (8)$$

If we consider the logarithm of the likelihood it becomes clear why including the intrinsic scatter differs from standard least squares minimization:

$$-2 \ln \mathcal{L} = 2 \sum_{i=1}^n \ln w_i + \sum_{i=1}^n \left(\frac{y_i - f(x_i; a_j)}{w_i} \right)^2 + C, \quad (9)$$

where the second term corresponds to the usual χ^2 and C is a constant. If there is no intrinsic scatter the first term is a constant for a given data set and the likelihood is maximized by minimizing χ^2 . However, the first term cannot be ignored if intrinsic scatter is included as a free parameter.

Table 4. SZ measurements

(1) name	(2) r_{2500}^{SZ} [h_{70}^{-1} kpc]	(3) Y [10^{-10}]	(4) $M^{\text{proj}}(< r_{2500}^{\text{SZ}})$ [$10^{14} h_{70}^{-1} M_{\odot}$]	(5) Θ_{500}^{X} [h_{70}^{-1} Mpc]	(6) Y_{PSX} [10^{-10}]	(7) $M^{\text{proj}}(< \Theta_{500}^{\text{X}})$ [$10^{14} h_{70}^{-1} M_{\odot}$]
A68	616	1.01 ± 0.16	5.0 ± 0.8			
A115N				1.22	4.27 ± 0.58	6.5 ± 1.5
A209				1.14	4.5 ± 0.4	8.9 ± 1.5
A267	484	0.72 ± 0.10	3.4 ± 0.5			
A370	508	0.71 ± 0.09	5.9 ± 0.8			
A520				1.24	3.9 ± 0.5	8.2 ± 1.7
A586	529	1.03 ± 0.14	2.7 ± 0.6			
A611	482	0.54 ± 0.06	3.2 ± 0.6			
A697	568	1.67 ± 0.19	4.8 ± 0.5	1.28	4.3 ± 0.4	12.7 ± 1.7
A963				1.11	1.6 ± 0.3	5.5 ± 1.5
A1689	664	3.79 ± 0.32	8.1 ± 0.8	1.38	6.0 ± 0.7	16.3 ± 1.9
A1758W				1.26	2.6 ± 0.3	12.8 ± 1.8
A1763				1.22	3.8 ± 0.4	11.2 ± 1.7
A1835	672	2.09 ± 0.17	6.5 ± 0.8			
A1914	660	3.01 ± 0.25	4.6 ± 0.7	1.30	4.8 ± 0.5	8.3 ± 1.5
A2111	518	0.95 ± 0.21	3.6 ± 0.5			
A2163	682	6.89 ± 0.65	6.8 ± 0.9	1.52	14.6 ± 0.6	15.0 ± 2.4
A2204	671	4.43 ± 0.51	6.2 ± 0.9	1.44	6.4 ± 0.6	12.0 ± 1.9
A2218	581	1.94 ± 0.19	4.4 ± 0.7	1.12	3.7 ± 0.3	7.1 ± 1.4
A2219				1.38	7.2 ± 0.4	12.8 ± 2.0
A2259	476	0.82 ± 0.30	1.8 ± 0.5			
A2261	525	1.34 ± 0.16	5.3 ± 0.5	1.33	4.1 ± 0.4	16.2 ± 1.6
A2390				1.39	4.7 ± 0.4	12.3 ± 1.9
MS0015.9+1609	507	0.73 ± 0.06	6.7 ± 0.8			
MS0451.6-0305	526	0.66 ± 0.05	3.7 ± 0.9			
MS0906.5+1110				1.12	2.3 ± 0.4	9.3 ± 1.6
MS1358.4+6245	539	0.56 ± 0.08	3.9 ± 0.6			
RX J1347.5-1145	706	1.61 ± 0.18	7.3 ± 1.2			
MACS J0717.5+3745				1.36	2.3 ± 0.3	23.5 ± 3.7
CIZA J1938+54				1.19	2.6 ± 0.2	10.8 ± 1.8

Column 2: r_{2500} as determined by Bonamente et al. (2008) from a joint analysis of X-ray and SZ data; Column 3: integrated Compton y -parameter from Bonamente et al. (2008); Column 4: the projected weak lensing mass within r_{2500}^{SZ} ; Column 5: the value for Θ_{500} from Planck Collaboration et al. (2011); Column 6: the integrated Compton Y -parameter within $5\Theta_{500}^{\text{X}}$ from Planck Collaboration et al. (2011); Column 7: projected weak lensing mass within Θ_{500}^{X} .

5.2 SZE measurements

The inverse Compton scattering of Cosmic Microwave Background (CMB) photons by the hot electrons in the intra-cluster medium results in a small distortion of the CMB spectrum, known as the Sunyaev-Zel'dovich effect (SZE; Sunyaev & Zel'dovich 1970). Depending on the observed frequency this leads to a reduction or increase in the brightness of the CMB at the location of the cluster (see e.g. Birkinshaw 1999). The surface brightness of the effect does not depend on redshift. As a consequence, it is (almost) as easy to detect high redshift clusters as it is to find them at lower redshifts. It is for this reason that the SZE has developed into an important technique to search for clusters of galaxies with the aim to constrain cosmological parameters (e.g. Carlstrom et al. 2002). A number of dedicated surveys have started to release results (e.g., Williamson et al. 2011; Marriage et al. 2011).

An additional benefit of SZ observations is the fact that the amplitude of the SZE, quantified by the integrated Compton y -parameter Y , is expected to be a good measure of the cluster mass. It is, however, still sensitive to the clus-

ter physics (e.g., McCarthy et al. 2003a,b) and thus needs to be calibrated observationally, ideally using weak gravitational lensing. For instance High et al. (2012) present the first weak lensing masses from dedicated follow-up observations for clusters discovered by the South Pole Telescope (SPT; Carlstrom et al. (2011)).

The first comparison of the SZE signal to lensing masses was presented in Marrone et al. (2009) who found a fairly large scatter using a sample of 14 massive clusters. The lensing masses, however, were based on HST observations covering only the cluster cores. This complicates the mass estimates and might lead to increased scatter (Hoekstra et al. 2002). More recently, Marrone et al. (2011) compared the SZE signal for 18 clusters to weak lensing masses determined by Okabe et al. (2010a) using Subaru wide field imaging data. The resulting scaling relation is in good agreement with earlier studies that assumed hydrostatic equilibrium. Marrone et al. (2011) find that a scatter of $\sim 20\%$ in weak lensing mass at fixed Y_{SZ} , although they note the scatter depends whether clusters are classified as disturbed or not.

In this section we compare our weak lensing masses to available measurements of the SZE signal from the lit-

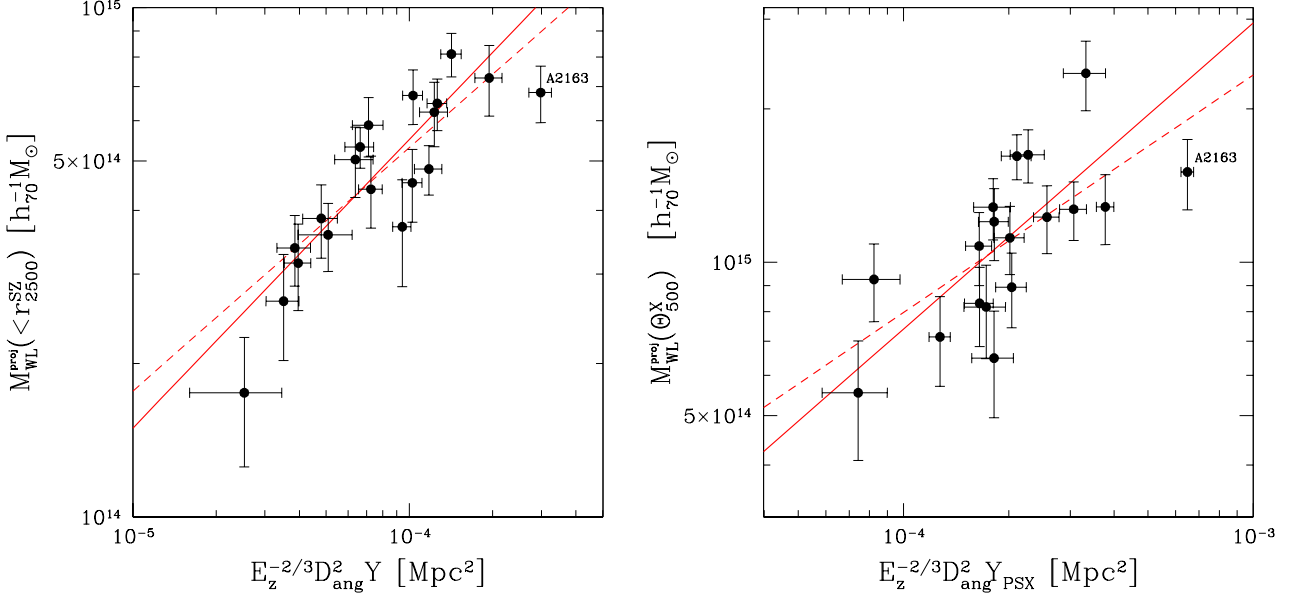


Figure 5. *left panel:* Plot of the projected weak lensing mass as a function of SZ signal. The mass is measured within an aperture of radius r_{2500}^{SZ} as determined by Bonamente et al. (2008) based on a joint analysis of X-ray and SZ data. The solid red line indicates the best fit power law model when the merging cluster A2163 (indicated) is excluded, whereas the dashed line is for the full sample. *Right panel:* Weak lensing mass within Θ_{500}^X as a function of projected Y from Planck Collaboration et al. (2011).

erature. We consider two samples, which partly overlap. Bonamente et al. (2008) present results for 38 massive clusters with BIMA and OVRO, 19 of which overlap with our sample. The second comparison is with the overlap of 18 clusters that were released in Planck Collaboration et al. (2011) as part of the *Planck* early results. Our aim is not to calibrate the scaling relations but to examine the potential of the SZE signal as a mass-proxy. The derivation of a useful scaling relation would require the apertures for the SZE results to be matched to the lensing radii, as is done for the X-ray observation in Mahdavi et al. (2012).

Bonamente et al. (2008) list their estimates for r_{2500}^{SZ} , based on a joint analysis of the available SZ and X-ray data. Their results are reproduced in Table 4. As the SZ measurement is a projected quantity (although not as extreme as the lensing signal), we compare to the projected lensing masses within an aperture r_{2500}^{SZ} , which are also listed in Table 4. Assuming a constant gas fraction and self-similarity, the SZ signal Y scales with mass as $M^{5/3} \propto D_A^2 E(z)^{-2/3} Y$ (e.g. McCarthy et al. 2003a; Bonamente et al. 2008). We assume this holds and take $D_A^2 E(z)^{-2/3} Y$ as the proxy for mass. The left panel of Figure 5 shows the projected lensing mass within r_{2500}^{SZ} as a function of the SZ signal from Bonamente et al. (2008).

We fit a power law model to the measurements, following the procedure described in §5.1. For a pivot value $D_A^2 E(z)^{-2/3} Y = 10^{-4}$ we find a best fit normalization of $M_0 = (5.16 \pm 0.24) \times 10^{14} h_{70}^{-1} M_\odot$ and a slope $\alpha = 0.48_{-0.07}^{+0.08}$, somewhat shallower than $\alpha = 0.6$ expected from the self-similar model. We obtain an intrinsic scatter of $12 \pm 5\%$ in mass for fixed Y . Note that our scatter is lower, but consistent with the values found by Marrone et al. (2011). The merging cluster A2163 is the main outlier and if we remove

Table 5. Best fit parameters of the SZE scaling relations

Bonamente	all	without A2163
$\sigma_{\log(Y M)}$	$0.10_{-0.04}^{+0.05}$	$0.06_{-0.06}^{+0.05}$
M_0	5.31 ± 0.24	5.51 ± 0.25
α	$0.48_{-0.07}^{+0.08}$	$0.57_{-0.08}^{+0.09}$
$\sigma_{\log(M Y)}$	0.05 ± 0.02	$0.04_{-0.04}^{+0.02}$
M_0	5.16 ± 0.24	5.43 ± 0.25
α	0.46 ± 0.07	$0.55_{-0.08}^{+0.09}$
<i>Planck</i>	all	without A2163
$\sigma_{\log(Y M)}$	$0.17_{-0.06}^{+0.09}$	$0.12_{-0.05}^{+0.07}$
M_0	11.0 ± 0.7	11.2 ± 0.7
α	$0.47_{-0.09}^{+0.11}$	$0.60_{-0.12}^{+0.14}$
$\sigma_{\log(M Y)}$	$0.076_{-0.022}^{+0.025}$	$0.074_{-0.023}^{+0.026}$
M_0	10.4 ± 0.6	10.6 ± 0.6
α	0.45 ± 0.11	0.56 ± 0.16

For the comparison with the measurements from Bonamente et al. (2008), M_0 is the normalization of the best fit power law with slope α to the projected weak lensing aperture mass within r_{2500}^{SZ} in units of $10^{14} h_{70}^{-1} M_\odot$, for a pivot $D_A^2 E(z)^{-2/3} Y = 10^{-4}$. We present parameters for a log-normal intrinsic scatter in Y for fixed mass, $\sigma_{\log(Y|M)}$ and vice versa, where we use the logarithm with base 10. For the comparison with the *Planck* result from Planck Collaboration et al. (2011) we use a pivot of 2×10^{-4} . For both samples we present results for the full sample and when Abell 2163 is excluded.

this cluster the results are consistent with no intrinsic scatter and the slope steepens to $\alpha = 0.57_{-0.08}^{+0.09}$ in agreement with the self-similar prediction and the slope of $0.60_{-0.06}^{+0.08}$ found by Bonamente et al. (2008) for their full sample.

Planck Collaboration et al. (2011) provide the integrated y -parameter within an aperture of radius $5\Theta_{500}^X$, where Θ_{500}^X is determined from X-ray observations by Piffaretti et al. (2011). Table 4 lists the *Planck* measurements and our projected lensing masses within Θ_{500}^X . The right panel of Figure 5 shows the weak lensing mass within this radius as a function for the SZE signal measured by Planck Collaboration et al. (2011). For these data we choose a pivot value $D_A^2 E(z)^{-2/3} Y = 2 \times 10^{-4}$, which gives a best fit normalization of $M_0 = (10.4 \pm 0.6) \times 10^{14} h_{70}^{-1} M_\odot$ and a slope $\alpha = 0.45 \pm 0.11$. The intrinsic scatter is $19_{-6}^{+7}\%$ in mass for fixed Y , consistent with the result for the Bonamente et al. (2008) sample and Marrone et al. (2011). As before, omitting A2163 from the analysis steepens the slope to $\alpha = 0.56 \pm 0.16$.

6 CONCLUSIONS

The Canadian Cluster Comparison Project targeted 50 massive X-ray luminous clusters of galaxies with redshifts $0.15 < z < 0.55$, with the aim of studying the scaling relations between cluster mass and baryonic tracers and to probe the cluster-to-cluster variation in the thermal properties of the hot intracluster medium. In this paper we present the results of our weak lensing analysis of deep wide-field imaging data obtained using the CFHT.

To ensure a significant detection of the lensing signal, clusters with an ASCA temperature of $T_X > 5\text{keV}$ from Horner (2001) were the main targets of the CCCP. This led to an overrepresentation of $z \sim 0.2$ clusters. Although the sample lacks a well-defined selection function, it appears to be representative, based on a comparison of the the $L_X - T_X$ relation (Mahdavi et al. 2012). We include two additional clusters that were located in the observed field-of-view. Hence we determine weak lensing masses for a total sample of 52 clusters of galaxies. We update the masses for 20 clusters studied previously in Hoekstra (2007), using the mass-concentration relation from Duffy et al. (2008) and present new results for 32 clusters observed with MegaCam.

We measure the lensing signal out to large radii, which allows us to determine aperture masses, which are nearly model-independent. To allow comparison with other observables we deproject the masses. We also fit NFW models to the data and explore the sensitivity of our results to the adopted mass-concentration relation. The values of M_{500} based on the aperture masses are robust, with a 20% increase (decrease) in the normalization of $c(M)$ resulting in a 4% increase (6% decrease) in the mass. The aperture masses agree well with the results from fitting NFW models. Although we cannot rule out a lower normalization, a significant increase in the concentration at a given mass leads to inconsistent values for M_{500} when comparing the masses from the NFW fit to the aperture masses.

The aperture masses are the reference for the comparison of cluster properties at other wavelengths. The scaling relation between a range of X-ray properties and lensing mass is presented in Mahdavi et al. (2012). In this paper we limit the comparison to published measurements of the Sunyaev-Zel'dovich (SZE) effect. We study a sample of 19 clusters that overlap with the study of Bonamente et al.

(2008) and another sample of 18 cluster that were observed by *Planck* (Planck Collaboration et al. 2011).

The SZE signal correlated well with the projected lensing mass. For both samples we find a best fit slope of the power law scaling relation that is lower than the value of $\alpha = 0.6$ for self-similar models. However, when the merging cluster A2163 is excluded, in both cases the slopes are in agreement with the self-similar prediction. We find an intrinsic scatter of $12 \pm 5\%$ in projected mass (M_{2500}) for fixed Y for the clusters that overlap with Bonamente et al. (2008). The comparison with the *Planck* results (Planck Collaboration et al. 2011) yields an intrinsic scatter in projected mass (M_{500}) of $19_{-6}^{+7}\%$ at fixed Y .

The scatter agrees well with the results from Marrone et al. (2011) and is comparable to the scatter in the scaling relations with (more expensive) X-ray observables such as hydrostatic mass and temperature (e.g., Mahdavi et al. 2012; Okabe et al. 2010b). This demonstrates that the SZE signal is a competitive proxy for cluster mass.

We thank Edo van Uitert for a careful reading of the manuscript. HH acknowledges support from the Netherlands organisation for Scientific Research (NWO) through VIDI grant 639.042.814; HH and CB acknowledge support from Marie Curie IRG Grant 230924. We also acknowledge support by the National Science and Engineering Research Council (NSERC) and the Canadian Foundation for Innovation (CFI). This research used the facilities of the Canadian Astronomy Data Centre operated by the National Research Council of Canada with the support of the Canadian Space Agency.

REFERENCES

- Allen S. W., Evrard A. E., Mantz A. B., 2011, *ARA&A*, 49, 409
- Babul A., Balogh M. L., Lewis G. F., Poole G. B., 2002, *MNRAS*, 330, 329
- Bahé Y. M., McCarthy I. G., King L. J., 2012, *MNRAS*, 421, 1073
- Becker M. R., Kravtsov A. V., 2011, *ApJ*, 740, 25
- Bildfell C., Hoekstra H., Babul A., Mahdavi A., 2008, *MNRAS*, 389, 1637
- Bildfell C. et al., 2012, ArXiv e-prints
- Birkinshaw M., 1999, *Phys. Rep.*, 310, 97
- Bonamente M., Joy M., LaRoque S. J., Carlstrom J. E., Nagai D., Marrone D. P., 2008, *ApJ*, 675, 106
- Bridle S. et al., 2010, *MNRAS*, 405, 2044
- Bullock J. S., Kolatt T. S., Sigad Y., Somerville R. S., Kravtsov A. V., Klypin A. A., Primack J. R., Dekel A., 2001, *MNRAS*, 321, 559
- Carlberg R. G., Yee H. K. C., Ellingson E., Abraham R., Gravel P., Morris S., Pritchett C. J., 1996, *ApJ*, 462, 32
- Carlstrom J. E. et al., 2011, *PASP*, 123, 568
- Carlstrom J. E., Holder G. P., Reese E. D., 2002, *ARA&A*, 40, 643
- Corless V. L., King L. J., 2007, *MNRAS*, 380, 149
- Cypriano E. S., Sodr e, Jr. L., Kneib J.-P., Campusano L. E., 2004, *ApJ*, 613, 95

- Dahle H., Kaiser N., Irgens R. J., Lilje P. B., Maddox S. J., 2002, *ApJS*, 139, 313
- David L. P., Kempner J., 2004, *ApJ*, 613, 831
- Duffy A. R., Schaye J., Kay S. T., Dalla Vecchia C., 2008, *MNRAS*, 390, L64
- Duffy A. R., Schaye J., Kay S. T., Dalla Vecchia C., Battye R. A., Booth C. M., 2010, *MNRAS*, 405, 2161
- Ebeling H., Edge A. C., Mantz A., Barrett E., Henry J. P., Ma C. J., van Speybroeck L., 2010, *MNRAS*, 407, 83
- Ettori S., Gastaldello F., Leccardi A., Molendi S., Rossetti M., Buote D., Meneghetti M., 2010, *A&A*, 524, A68
- Fahlman G., Kaiser N., Squires G., Woods D., 1994, *ApJ*, 437, 56
- Feldmeier J. J., Mihos J. C., Morrison H. L., Harding P., Kaib N., Dubinski J., 2004, *ApJ*, 609, 617
- Fu L. et al., 2008, *A&A*, 479, 9
- Gioia I. M., Maccacaro T., Schild R. E., Wolter A., Stocke J. T., Morris S. L., Henry J. P., 1990, *ApJS*, 72, 567
- Giovannini G., Tordi M., Feretti L., 1999, *New Astronomy*, 4, 141
- Gladders M. D., Yee H. K. C., 2005, *ApJS*, 157, 1
- Heymans C. et al., 2006, *MNRAS*, 368, 1323
- High F. W. et al., 2012, *ArXiv e-prints*
- Hoekstra H., 2001, *A&A*, 370, 743
- Hoekstra H., 2003, *MNRAS*, 339, 1155
- Hoekstra H., 2007, *MNRAS*, 379, 317
- Hoekstra H., Donahue M., Conselice C. J., McNamara B. R., Voit G. M., 2011a, *ApJ*, 726, 48
- Hoekstra H., Franx M., Kuijken K., 2000, *ApJ*, 532, 88
- Hoekstra H., Franx M., Kuijken K., Squires G., 1998, *ApJ*, 504, 636
- Hoekstra H., Franx M., Kuijken K., van Dokkum P. G., 2002, *MNRAS*, 333, 911
- Hoekstra H., Hartlap J., Hilbert S., van Uitert E., 2011b, *MNRAS*, 412, 2095
- Hoekstra H. et al., 2006, *ApJ*, 647, 116
- Hoekstra H., Yee H. K. C., Gladders M. D., 2004, *ApJ*, 606, 67
- Horner D. J., 2001, PhD thesis, University of Maryland College Park
- Ilbert O. et al., 2006, *A&A*, 457, 841
- Jee M. J. et al., 2011, *ApJ*, 737, 59
- Jee M. J., Mahdavi A., Hoekstra H., Babul A., Dalcanton J. J., Carroll P., Capak P., 2012, *ApJ*, 747, 96
- Johnston D. E. et al., 2007, *ArXiv e-prints*
- Jones M. E. et al., 2005, *MNRAS*, 357, 518
- Kaiser N., 1986, *MNRAS*, 222, 323
- Kaiser N., Squires G., 1993, *ApJ*, 404, 441
- Kaiser N., Squires G., Broadhurst T., 1995, *ApJ*, 449, 460
- Kempner J. C., Sarazin C. L., 2001, *ApJ*, 548, 639
- Kitching T. D. et al., 2012, *ArXiv e-prints*
- Koester B. P. et al., 2007, *ApJ*, 660, 239
- Komatsu E. et al., 2009, *ApJS*, 180, 330
- Lewis G. F., Babul A., Katz N., Quinn T., Hernquist L., Weinberg D. H., 2000, *ApJ*, 536, 623
- Luppino G. A., Kaiser N., 1997, *ApJ*, 475, 20
- Macciò A. V., Dutton A. A., van den Bosch F. C., 2008, *MNRAS*, 391, 1940
- Mahdavi A., Hoekstra H., Babul A., Balam D. D., Capak P. L., 2007, *ApJ*, 668, 806
- Mahdavi A., Hoekstra H., Babul A., et al., 2012, submitted
- Mahdavi A., Hoekstra H., Babul A., Henry J. P., 2008, *MNRAS*, 384, 1567
- Mandelbaum R., Seljak U., Kauffmann G., Hirata C. M., Brinkmann J., 2006, *MNRAS*, 368, 715
- Marriage T. A. et al., 2011, *ApJ*, 737, 61
- Marrone D. P. et al., 2011, eprint arXiv:1107.5115
- Marrone D. P. et al., 2009, *ApJ*, 701, L114
- Massey R. et al., 2007, *MNRAS*, 376, 13
- McCarthy I. G., Babul A., Holder G. P., Balogh M. L., 2003a, *ApJ*, 591, 515
- McCarthy I. G., Balogh M. L., Babul A., Poole G. B., Horner D. J., 2004, *ApJ*, 613, 811
- McCarthy I. G., Holder G. P., Babul A., Balogh M. L., 2003b, *ApJ*, 591, 526
- Meneghetti M., Rasia E., Merten J., Bellagamba F., Ettori S., Mazzotta P., Dolag K., Marri S., 2010, *A&A*, 514, A93
- Metzler C. A., White M., Loken C., 2001, *ApJ*, 547, 560
- Morandi A., Limousin M., 2012, *MNRAS*, 421, 3147
- Nagai D., Vikhlinin A., Kravtsov A. V., 2007, *ApJ*, 655, 98
- Navarro J. F., Frenk C. S., White S. D. M., 1996, *ApJ*, 462, 563
- Navarro J. F., Frenk C. S., White S. D. M., 1997, *ApJ*, 490, 493
- Neto A. F. et al., 2007, *MNRAS*, 381, 1450
- Okabe N., Takada M., Umetsu K., Futamase T., Smith G. P., 2010a, *PASJ*, 62, 811
- Okabe N., Umetsu K., 2008, *PASJ*, 60, 345
- Okabe N., Zhang Y.-Y., Finoguenov A., Takada M., Smith G. P., Umetsu K., Futamase T., 2010b, *ApJ*, 721, 875
- Perlmutter S. et al., 1999, *ApJ*, 517, 565
- Piffaretti R., Arnaud M., Pratt G. W., Pointecouteau E., Melin J.-B., 2011, *A&A*, 534, A109
- Planck Collaboration et al., 2011, *A&A*, 536, A8
- Prada F., Klypin A. A., Cuesta A. J., Betancort-Rijo J. E., Primack J., 2011, *ArXiv e-prints*
- Ragozzine B., Clowe D., Markevitch M., Gonzalez A. H., Bradač M., 2012, *ApJ*, 744, 94
- Reiprich T. H., Böhringer H., 2002, *ApJ*, 567, 716
- Riess A. G. et al., 1998, *AJ*, 116, 1009
- Schrabback T. et al., 2010, *A&A*, 516, A63
- Smail I., Ellis R. S., Dressler A., Couch W. J., Oemler, Jr. A., Sharples R. M., Butcher H., 1997, *ApJ*, 479, 70
- Sunyaev R. A., Zel'dovich Y. B., 1970, *Ap&SS*, 7, 3
- Umetsu K., Broadhurst T., Zitrin A., Medezinski E., Hsu L.-Y., 2011, *ApJ*, 729, 127
- van Uitert E., Hoekstra H., Velandier M., Gilbank D. G., Gladders M. D., Yee H. K. C., 2011, *A&A*, 534, A14
- Weiner B. J. et al., 2006, *ApJ*, 653, 1049
- Williamson R. et al., 2011, *ApJ*, 738, 139
- Yee H. K. C., Ellingson E., Carlberg R. G., 1996, *ApJS*, 102, 269
- Zitrin A. et al., 2011, *ApJ*, 742, 117
- Zitrin A. et al., 2010, *MNRAS*, 408, 1916